



HAL
open science

Analysis of the radar vegetation index and potential improvements

Christoph Szigarski, Thomas Jagdhuber, Martin Baur, Christian Thiel, Marie Parrens, Jean-Pierre Wigneron, Maria Piles, Dara Entekhabi

► **To cite this version:**

Christoph Szigarski, Thomas Jagdhuber, Martin Baur, Christian Thiel, Marie Parrens, et al.. Analysis of the radar vegetation index and potential improvements. *Remote Sensing*, 2018, 10 (11), pp.1-15. 10.3390/rs10111776 . hal-02621455

HAL Id: hal-02621455

<https://hal.inrae.fr/hal-02621455v1>

Submitted on 26 May 2020

HAL is a multi-disciplinary open access archive for the deposit and dissemination of scientific research documents, whether they are published or not. The documents may come from teaching and research institutions in France or abroad, or from public or private research centers.




L'archive ouverte pluridisciplinaire **HAL**, est destinée au dépôt et à la diffusion de documents scientifiques de niveau recherche, publiés ou non, émanant des établissements d'enseignement et de recherche français ou étrangers, des laboratoires publics ou privés.



Distributed under a Creative Commons Attribution 4.0 International License

Article

Analysis of the Radar Vegetation Index and Potential Improvements

Christoph Szigarski ^{1,*}, Thomas Jagdhuber ¹ , Martin Baur ², Christian Thiel ³, Marie Parrens ^{4,5} , Jean-Pierre Wigneron ⁶, Maria Piles ⁷  and Dara Entekhabi ⁸

¹ German Aerospace Center, Microwaves and Radar Institute, P.O. Box 1116, 82234 Wessling, Germany; thomas.jagdhuber@dlr.de

² Bayreuth Center for Ecology and Environmental Research, University of Bayreuth, Universitätsstraße 30, 95447 Bayreuth, Germany; martin.baur@uni-bayreuth.de

³ German Aerospace Center, Institute of Data Science, Mälzerstraße 3, 07745 Jena, Germany; christian.thiel@dlr.de

⁴ Cesbio, 18 avenue Edouard Belin, 31401 Toulouse, France; marie.parrens@cesbio.cnrs.fr

⁵ E.I Purpan, 75 voie du TOEC, BP57611, 31076 Toulouse CEDEX 3, France

⁶ INRA, Centre de Bordeaux Aquitaine, 71 avenue E. Bourlaux, 33882 Villenave d'Ornon CEDEX, France; jean-pierre.wigneron@inra.fr

⁷ Image Processing Lab, Parc Científic, University of Valencia, 46980 Paterna Valencia, Spain; maria.piles@uv.es

⁸ Department of Civil and Environmental Engineering, MIT, Vassar Street 15, Cambridge, MA 02139, USA; darae@mit.edu

* Correspondence: chszigarski@aol.de; Tel.: +49-176-47194985

Received: 7 October 2018; Accepted: 7 November 2018; Published: 9 November 2018



Abstract: The Radar Vegetation Index (RVI) is a well-established microwave metric of vegetation cover. The index utilizes measured linear scattering intensities from co- and cross-polarization and is normalized to ideally range from 0 to 1, increasing with vegetation cover. At long wavelengths (L-band) microwave scattering does not only contain information coming from vegetation scattering, but also from soil scattering (moisture & roughness) and therefore the standard formulation of RVI needs to be revised. Using global level SMAP L-band radar data, we illustrate that RVI runs up to 1.2, due to the pre-factor in the standard formulation not being adjusted to the scattering mechanisms at these low frequencies. Improvements on the RVI are subsequently proposed to obtain a normalized value range, to remove soil scattering influences as well as to mask out regions with dominant soil scattering at L-band (sparse or no vegetation cover). Two purely vegetation-based RVIs (called RVII and RVIII), are obtained by subtracting a forward modeled, attenuated soil scattering contribution from the measured backscattering intensities. Active and passive microwave information is used jointly to obtain the scattering contribution of the soil, using a physics-based multi-sensor approach; simulations from a particle model for polarimetric vegetation backscattering are utilized to calculate vegetation-based RVI-values without any soil scattering contribution. Results show that, due to the pre-factor in the standard formulation of RVI the index runs up to 1.2, atypical for an index normally ranging between zero and one. Correlation analysis between the improved radar vegetation indices (standard RVI and the indices with potential improvements RVII and RVIII) are used to evaluate the degree of independence of the indices from surface roughness and soil moisture contributions. The improved indices RVII and RVIII show reduced dependence on soil roughness and soil moisture. All RVI-indices examined indicate a coupled correlation to vegetation water content (plant moisture) as well as leaf area index (plant structure) and no single dependency, as often assumed. These results might improve the use of polarimetric radar signatures for mapping global vegetation.

Keywords: microwaves; radiometer; radar; vegetation index; soil scattering; roughness; soil moisture; SMAP; SMOS

1. Introduction

Mapping the density of woody vegetation cover at large scales is required in applications such as estimating terrestrial carbon stocks. Vegetation dynamics are also linked to global climate processes [1,2]. The forest ecosystems exchange water, energy, carbon and other biogeochemical species with the atmosphere and especially play a critical role in atmospheric carbon dioxide uptake [2–4]. Continuous mapping of these ecosystems delivers crucial information to quantify and understand change in the environment from local to global scales [1].

Over the past decades, remote sensing of vegetation cover has mainly been based on measurements in visible, near infrared and shortwave bands [1,5,6]. Optical and infrared indices have limitations associated with opacity of the atmosphere due to clouds, water vapor and aerosols. Active (send & receive) and passive (only receive) microwave remote sensing operates in a wavelength range between 1 mm and 1 m. Unlike optical and infrared, microwave remote sensing is independent from solar illumination and penetrates areas covered by clouds, haze and rain (study frequency: L-band at about 1.3 GHz [7]) [6,8]. They thus allow gap-free data streams for vegetation mapping.

Moreover, while optical methods mostly sense surface and top of canopy conditions, microwaves can penetrate into the vegetation canopy especially at longer wavelengths (e.g., L-band at about 21 cm wavelength). In this regard, observations in the microwave spectrum provide information related to plant moisture content and structure and offer a distinct view on plant conditions [5]. A parameter frequently used in vegetation mapping is the vegetation optical depth (VOD) [9], which can be retrieved for instance from AMSR or SMAP radiometer data. In order to use radar for mapping vegetation cover, a robust index is desirable. However, at longer wavelengths (e.g., L-band), microwave indices are potentially influenced by soil moisture and surface roughness contributions, also in presence of dense vegetation [10]. When applying microwave indices as in [11], these soil contaminations have not been taken into account, resulting in misleading interpretations.

One of the more established active microwave indices for mapping vegetation cover is the Radar Vegetation Index (RVI) [12]. A sensitivity analysis of RVI at L-band was presented in [13], and it has been utilized in studies such as [14–16]. In particular, prior investigations on RVI have compared it to optical-based measures like the Normalized Difference Vegetation Index (NDVI), indicating greenness of vegetation and Leaf Area Index (LAI), used to detect canopy layers from vegetation [14]. Also, the RVI index has been shown to be related to the Vegetation Water Content (VWC) [14–16] that is directly linked to the wetness of vegetation. Optical and infrared indices are however mostly sensitive to scattering and absorption on leaf surfaces. The influence of wetness (e.g., VWC) and structure (e.g., LAI) of a canopy on RVI is not yet understood sufficiently. In addition, the extent to which the RVI index is solely connected to vegetation at long wavelengths (e.g., L-band) is not fully known.

This study investigates the characteristics of the RVI and assesses the potential for its improvement. We investigate the degree to which RVI isolates the scattering by vegetation and is independent of soil surface reflectivity, soil moisture and roughness. In the following sections we analyze these characteristics of the RVI index and introduce two improved formulations using a multi-sensor (active-passive microwave) approach.

2. Test Sites and Experimental Data

2.1. Test Sites

Investigations regarding the RVI-value range are initially carried out at global level. Beside the investigation on global data, an in-depth study will be conducted over a few regions, in order to span the entire range of land cover types without biasing the results towards a few dominant land cover types. To define a set of suitable test sites, the following criteria are considered:

- Coverage of different climate and vegetation zones, based on the International Geosphere-Biosphere Programme (IGBP) classification from [17],
- Diversely vegetated areas to cover high and low RVI mean,
- Varying degrees of complexity in vegetation structure,
- Inclusion of areas with distinct vegetation cover,
- Availability of polarimetric radar data and auxiliary datasets.

The following sites are selected for the statistical analyses: Eastern U.S., Yucatan Peninsula, Sweden, East Europe, Eastern South Africa, Kalimantan and Southeast China (Figure 1). The dataset is compiled based on the above-mentioned criteria and includes vegetation canopies from: tropical climate with evergreen broadleaf forests, mangroves, nipa palms (Kalimantan, Central parts of Yucatan); warm temperate areas that grow deciduous broadleaf forests, mixed forests and cultivated patterns (Eastern Europe, Southeast of China, Eastern U.S.); warm temperate and fully humid lands covered by woody savannas and grassland (Eastern South Africa); continental and fully humid territories characterized by extensive deciduous broadleaf forest (Central Sweden); polar regions that contain robust needleleaf species and coverage by single pine and spruce trees.

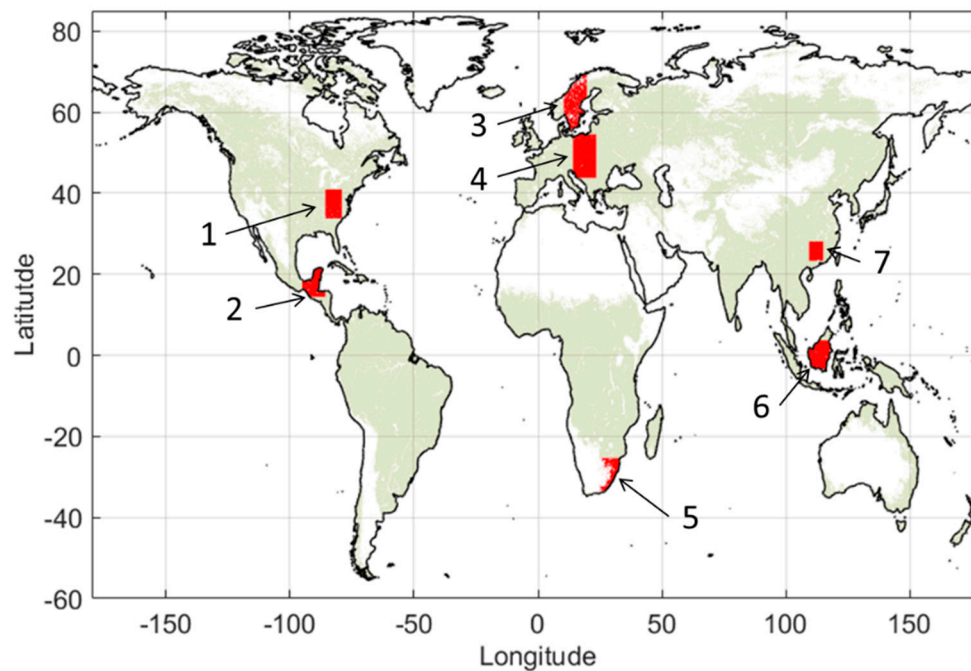


Figure 1. Locations of the in-depth test sites are marked as red polygons. The following sites are selected: Eastern U.S. (1), Yucatan Peninsula (2), Sweden (3), East Europe (4), Eastern South Africa (5), Kalimantan (6) and Southeast China (7). The light green color indicates the areas of dominant vegetation scattering (result of masking areas with dominant soil scattering (cf. Section 3)).

2.2. Experimental Data

The L-band, polarimetric, space-borne radar data acquired by the NASA SMAP mission (Soil Moisture Active Passive [7]) is the central dataset used in this study. The SMAP active-passive dataset was recorded from 13 April 2015 to 7 July 2015. This period begins with the post-launch start of science data acquisition by SMAP and ends on the date of the SMAP radar failure [7]. The used data is the global level 3 product (SPL3SMAP) [18] that contains the linear backscattering intensities for the polarizations HH, VV and aggregation of cross-polarizations (HV or VH) from the L-band radar on a 9 km grid, as well as soil moisture and vegetation optical depth from SMAP L-band radiometer retrievals on a 36 km grid for a global scale [7]. For the investigations of the RVI, time-averaged values (April to July 2015) were considered because of the short period of record.

In addition, soil roughness information (vertical component) from Parrens et al. [19] are used in the forward modelling of the surface scattering component. This dataset is computed from SMOS (Soil Moisture and Ocean Salinity [20]) L-band passive microwave observations with a spatial resolution of ~43 km at global scale for the year 2011 [21]. A gap-filling procedure using mean roughness values per IGBP land cover class is used to provide spatially continuous information, as suggested in [22]. This was necessary due to the data gaps in the original product of [19] caused by strong vegetation cover in regions where no soil roughness could be estimated.

Furthermore, the MODIS-based vegetation water content (VWC) [23] included in the SMAP product (SPL3SMAP) [18] is used for the correlation analysis in the results section. The MODIS-based leaf area index (LAI) [24] will be used in the same section. The LAI data were available for all study areas with 500 m spatial resolution gridded on 0.5° in latitude and longitude [25].

3. Modelling and Retrieval of Standard and Improved RVI

The radar vegetation index (RVI) has been used in a number of previous studies (e.g., [13,14]) mostly for predicting the growth level of crop vegetation over time [14]. The RVI, as firstly introduced by Kim & van Zyl, is a measure of volume scattering (from randomly oriented dipoles), a scattering mechanism usually caused by complex structural elements of vegetation (e.g., combination of leaves, branches & trunks). The index is defined as [26]:

$$RVI = \frac{8 \sigma_{HV}}{\sigma_{HH} + \sigma_{VV} + 2\sigma_{HV}}, \quad (1)$$

where σ_{HH} , σ_{HV} and σ_{VV} represent the measured linear backscattering intensities [-]. The 8 in the numerator is referred to the pre-factor in this study. The RVI is meant to be a normalized index that ideally varies between zero and one.

For L-band SAR applications at global scale it is likely that the measured quantities contain not only scattering from vegetation cover, but also from the soil underneath. This is especially critical for sparsely vegetated areas where there is soil backscattering in the co- and cross-polarizations. In some cases, the RVI may over- or under-estimate vegetation volume scattering because it is based on a ratio. Soil scattering contributions need to be removed from the measured intensities in (1). As stated in [14], the RVI should typically vary between zero and one. Values near zero should correspond to bare surfaces. Values near one should indicate a dense vegetation canopy. A previous study showed that the index tends to overestimate biomass in dry regions [13]. To gain insight into the behavior of the index, a polarimetric vegetation scattering forward model needs to be developed.

Scattering from a vegetation canopy can be modelled using a cloud of randomly oriented thin cylinders and discs with lossy dielectric properties [12]. A polarimetric spheroidal particle model is used here [27] to ensure flexibility for application to vegetation canopies with different structures and geometries. This model is driven by the particle anisotropy (A_p) and orientation distribution width (ψ) of the spheroidal particles that form the scattering canopy media. The particle anisotropy represents the main plant constituents (e.g., stem, branches, leaves) forming the uniformly shaped volume. The orientation distribution width embodies the degree of orientation and organization of the constituents within the volume. Further details of the model are given in [27,28]. The linear backscattering coefficients σ_{PP} [-], as a function of A_p [-] and ψ [rad], are given as follows [27]:

$$\sigma_{HH} = \frac{1}{1 + A_p^2} \cdot \frac{1}{8} (3A_p^2 + 2A_p + 3 + 4(A_p^2 - 1) \text{Sinc}(2\psi) + (A_p - 1)^2 \text{Sinc}(4\psi)), \quad (2)$$

$$\sigma_{VV} = \frac{1}{1 + A_p^2} \cdot \frac{1}{8} (3A_p^2 + 2A_p + 3 - 4(A_p^2 - 1) \text{Sinc}(2\psi) + (A_p - 1)^2 \text{Sinc}(4\psi)), \quad (3)$$

$$\sigma_{HV} = \frac{1}{1 + A_p^2} \cdot \frac{1}{8} (A_p - 1)^2 (1 - \text{Sinc}(4\psi)). \quad (4)$$

The backscattering intensities are calculated using three sets of Ap -values, varying between zero and 10^6 (0–1; 1–100; 100– 10^6). The first set (0–1) capture particle shapes from vertical dipoles to spheres, the second (1–100) and third range (100– 10^6) simulate particles from spheres (values around 1) to horizontal dipoles (values that tend to infinity). The evaluation of the standard RVI index using the forward modelled linear backscattering intensities leads to an upper limit of 1.2 for the index. Analysis of the entire Ap - and ψ -range with the canopy model can result in an optimized pre-factor for the cross-polarization component within the RVI formulation (numerator in (1)). The optimization of this pre-factor can shift the resulting values of RVI to be confined in zero to one range. The standard pre-factor ($A = 8$) in (1) assumes randomly oriented dipoles that do not normalize the full range of potentially occurring σ_{HV} -intensities due to variety in vegetation shape and structure. The white line in Figure 2 marks the maximum of modelled σ_{HV} -values (0.125) from vegetation that can be normalized by the standard pre-factor of 8. The global maximum when modelled with the particle model was located at a higher value of 0.152. Therefore, the optimum pre-factor for an improved RVI is found to be 6.57.

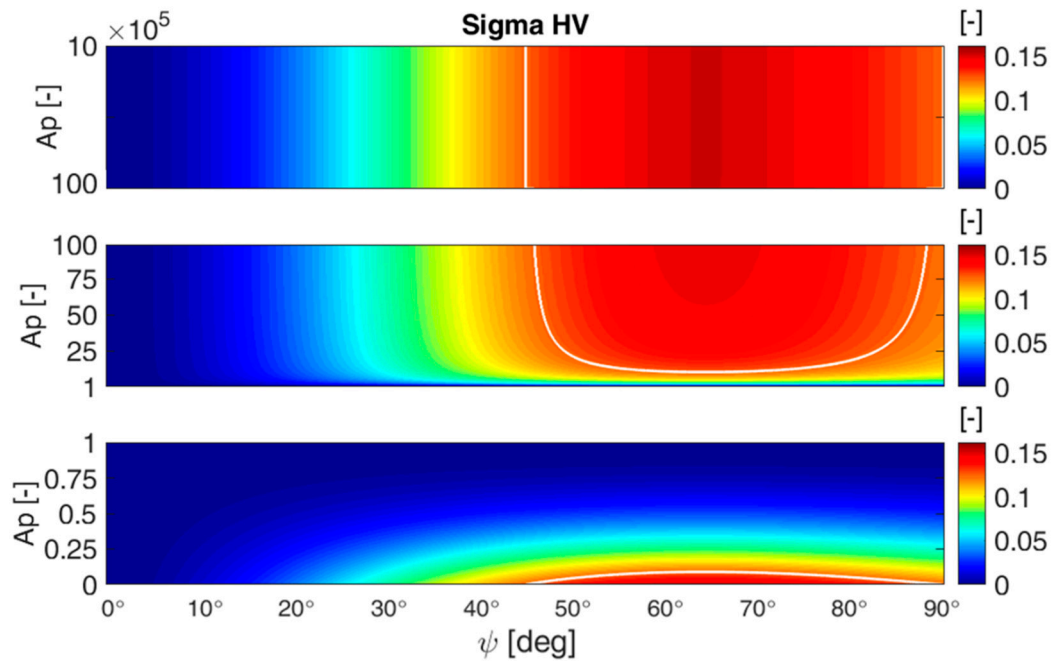


Figure 2. Density plot of modelled σ_{HV} -values [-] from (4) as a function of vegetation parameters ψ [rad] (orientation distribution width = degree of orientation in canopy) and Ap (particle anisotropy = plant shape) [-]. The white line indicates the maximum of modelled σ_{HV} -values (0.125) that can be normalized by the standard pre-factor of 8 in (1). The three panels correspond to different ranges of Ap (0–1; 1–100; 100– 10^6).

In addition to modelling the structural component of the RVI, we investigate the permittivity component of the forward vegetation scattering model. This modelling approach is still based on the variation in ψ , but starts on permittivity input level. To simulate the dielectric constant ϵ_v of the vegetation, the semi-physical method of Ulaby & El-Rayes is used [29]. The resulting complex dielectric constant ϵ_v is input to the modelling of the particle shape, leading to variations in the parameter Ap . This is done by solving the particle shape functions L_1 , L_2 for a given major ($x_1 = 0.01$ m) and minor axes ($x_2 = 0.05$ m) [30,31]:

$$L_1 = \begin{cases} \text{prolate} : \frac{1-e^2}{e^2} \left(-1 + \frac{1}{2e} \ln \frac{1+e}{1-e} \right) & x_1 > x_2 & e^2 = 1 - \frac{x_2^2}{x_1^2} \\ \text{oblate} : \frac{1-f^2}{f^2} \left(1 - \frac{1}{f} \arctan(f) \right) & x_1 < x_2 & f^2 = \frac{x_2^2}{x_1^2} - 1 \end{cases} \quad (5)$$

$$L_2 = \frac{1}{2} (1 - L_1). \quad (6)$$

Both functions differentiate between a prolate and an oblate scenario to capture the entire shape variation of the spheroidal particles. The particle anisotropy A_p can be calculated using a ratio of the polarizabilities ρ_{ee1} and ρ_{ee2} calculated from shape functions L_1 and L_2 [28]:

$$A_p = \frac{\rho_{ee1}}{\rho_{ee2}} = \frac{L_2 + 1/(\epsilon_r - 1)}{L_1 + 1/(\epsilon_r - 1)} \begin{cases} A_p < 1 & \text{oblate spheroids} \\ A_p = 1 & \text{spheres} \\ A_p > 1 & \text{prolate spheroids} \end{cases} \quad (7)$$

This enables the determination of the shape A_p in dependence of a permittivity input. Consequently, the RVI is simulated using the A_p - ψ model in (1) with the retrieved particle anisotropy A_p as well as the modelled orientation distribution width ψ (full extend: 0° to 90°). The conceptual workflow of the model-based RVI, starting at permittivity input level is shown in Figure 3.

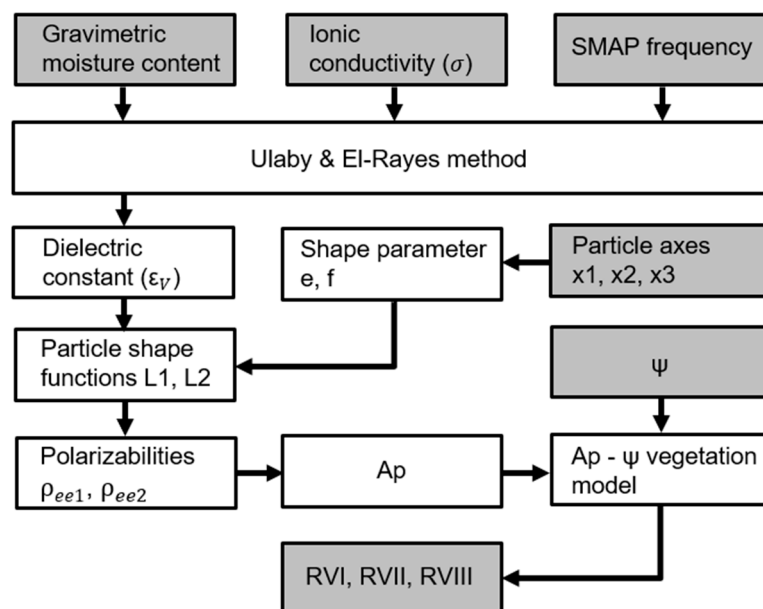


Figure 3. Conceptual workflow of the model-based RVI, starting at permittivity input level. Input and output parameters are marked in grey boxes.

The modelled results for the RVI are shown in Figure 4 (prolate scenario). For low ψ -values (20 – 30°) there are no variations of the RVI with increasing vegetation permittivity. With an increasingly complex vegetation structure (40 – 90°), there are the widest variations in RVI along vegetation permittivity (real & imaginary part). The variations of RVI for the distribution interval from 30 to 60° are similar and between 15 – 50 in real part and between 5 – 15 in imaginary part of the permittivity. It also clearly shows that only for very low permittivity (real & imaginary part), there are no variations of the RVI over this complexity range. The oblate scenario exhibited similar results (not shown).

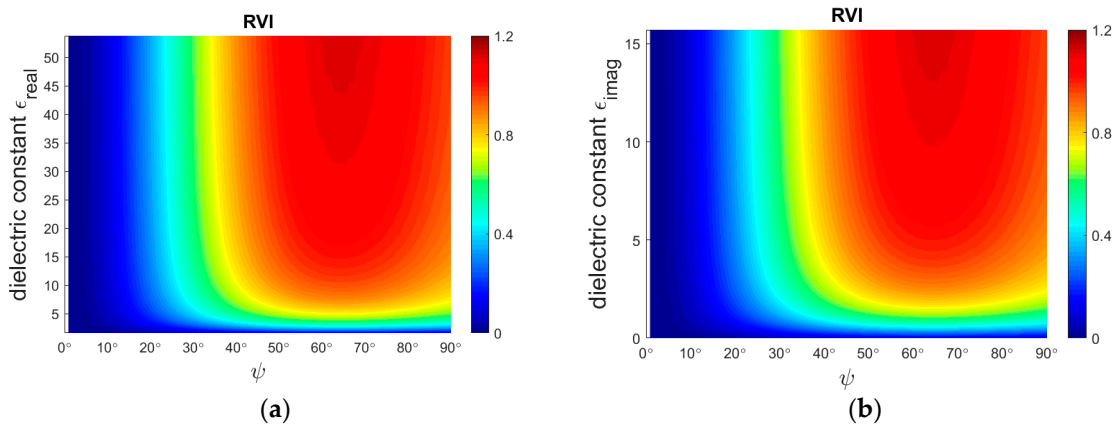


Figure 4. Density plots of modeled RVI [-] as a function of the vegetation structure parameter ψ [deg] and the complex dielectric constant ϵ_v [-] of vegetation (after Ulaby & El-Rayes [29]), split in real (a) and imaginary (b) part for the prolate spheroid scenario.

With the availability of the forward model of the σ_{HV} -component, there is now potential for improvements in the pre-factor of RVI (normalization of index). Further improvements are introduced by including an active-passive microwave-based correction for a soil scattering component within the cross polarization σ_{HV} in (1), originating from soil roughness effects [27]. This improvement is realized using a multi-sensor approach based on a forward modelling of the soil component. Hence, an improved definition of (1) is found given to be:

$$RVII = \frac{6.57(\sigma_{HV}^m - \sigma_{HV}^s \gamma^2)}{(\sigma_{HH}^m) + (\sigma_{VV}^m) + 2(\sigma_{HV}^m)}, \quad (8)$$

where the parameter γ represents the one-way attenuation of the soil signal while passing through the vegetation media. The one-way attenuation is derived from SMAP radiometer-based retrievals of vegetation optical depth (VOD), using the MT-DCA algorithm from [32]. The estimates are assumed polarization independent for L-band at global scales [32].

In (8) σ_{pq}^m is the measured linear backscattering intensities and σ_{pq}^s is the soil scattering intensity, originating from forward modelling. Here, the extended Bragg model is used [33]. This polarimetric bare soil scattering model for longer wavelength (L-band) requires input of the roughness and relative permittivity of the soil. The latter is obtained from passive microwave soil moisture retrievals (e.g., SMAP baseline algorithm), using the dielectric mixing model of Mironov & Fomin for the conversion to permittivity [22,34]. For the soil roughness input, a SMOS-based dataset is utilized, as introduced in Chapter 2.2. The conceptual workflow of the improved RVI (RVII and RVIII) retrieval is shown in Figure 5.

An alternative approach of incorporating corrections for soil contributions in (5) is that all measured input intensities are corrected for their respective soil scattering component. In this way, soil contribution terms σ^s need to be known for all co- and cross polarizations. The maximum soil correction of the measured intensities, is expressed as follows:

$$RVIII = \frac{6.57(\sigma_{HV}^m - \sigma_{HV}^s \gamma^2)}{(\sigma_{HH}^m - \sigma_{HH}^s \gamma^2) + (\sigma_{VV}^m - \sigma_{VV}^s \gamma^2) + 2(\sigma_{HV}^m - \sigma_{HV}^s \gamma^2)}. \quad (9)$$

However, the quality and spatial resolution of the RVII and RVIII can only be as good as its remotely-sensed (SMAP & SMOS) input data for σ_{pq}^s and γ . The improved indices incorporates ((8) and (9)) combine information from active and passive microwave sensor data.

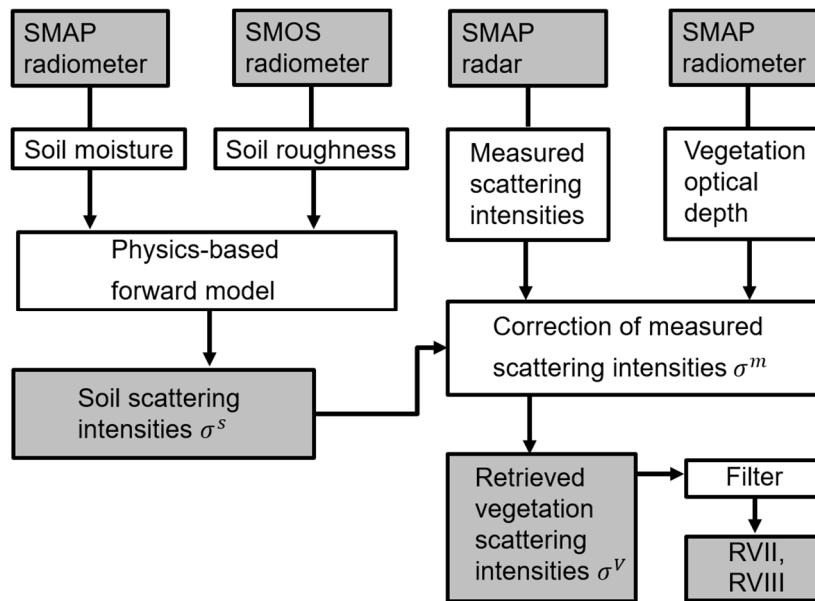


Figure 5. Conceptual workflow of retrieving the improved radar vegetation index (RVII) by a multi-sensor (active-passive microwave) approach. The input sensors and the output parameters are marked in grey boxes.

In addition to the correction of the soil scattering component, the original RVI and the improved indices (RVII and RVIII) need to be applied to the regions where they are valid (non-bare and non-ice and snow-covered surfaces). The definitions of the excluded regions are described in more detail in Section 4. The IGBP classification of land cover is used and the exclusion regions are shown in Figure 6. Bare soil and sparse vegetation regions (deserts, sparse shrublands and steppes) are not within the range of applicability of radar vegetation indices. If the removal of σ_{pq}^S from σ_{pq}^m led to negative values, an indicator of the dominance of soil scattering over vegetation scattering, the area is masked. This check for negative-valued intensities after removal of soil scattering is done for all polarizations.

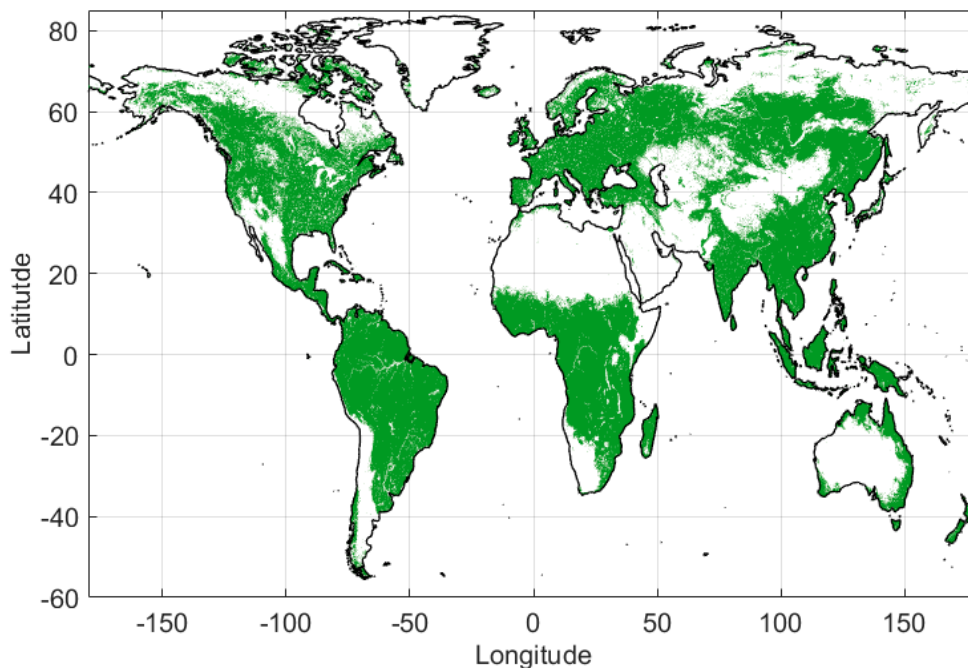


Figure 6. Retrieved mask of valid (dominant vegetation scattering) RVI-values (green) and excluded regions where soil scattering is dominant (white) at L-band.

In the next section correlations between standard and improved RVI with soil- and vegetation-related parameters are conducted in order to assess the degree to which RVI is an indicator of vegetation structure and permittivity and independent of surface soil reflectivity. The model analyses in this section showed that there is permittivity as well as structure dependence in radar vegetation indices. Therefore, the following parameters are selected for a comparison: volumetric soil moisture and vegetation water content (VWC) for permittivity dependency; vertical surface roughness (k_s) and leaf area index (LAI) for structure related correlation.

4. Results

4.1. Global Results

The global overview of the standard RVI, calculated with (1) and using SMAP radar data is shown in Figure 7a. The Radar Vegetation Index defined in (1) shows a global pattern corresponding to known global distribution of land cover. It is based on the short period (April to July 2015) where the SMAP radar was operating. But cloud cover and illumination do not result in any data losses because it is based on L-band radar measurements. The panel in Figure 7b shows that the index can exceed the value of one. Especially in the tropical latitudes (e.g., Amazon basin) the maximum values reach up to 1.2. The global maximum of the histogram in Figure 7b is around 0.8 and there is also a local maximum close to one. There may be an overall overestimation of RVI towards higher values (>0.8 [-]), which was already reported empirically in [14] and affirmed and analyzed with forward modelling of a polarimetric vegetation scattering model in the previous section. The mask in Figure 6 is not applied to RVI because in this study we used the RVI-values in the excluded region to diagnose soil surface scattering and reflectivity contributions.

The pre-factor of the numerator in (1) can result in improved dynamic range and interpretability of RVI. Figure 8 illustrates the result of the improved RVI (RVII) computed with (8). Figure 9 shows the results of the fully corrected RVI (RVIII) calculated with (9). The incorporation of the forward model-derived pre-factor and the active-passive microwave-based removal of the attenuated soil contribution leads to an indexing between zero and one.

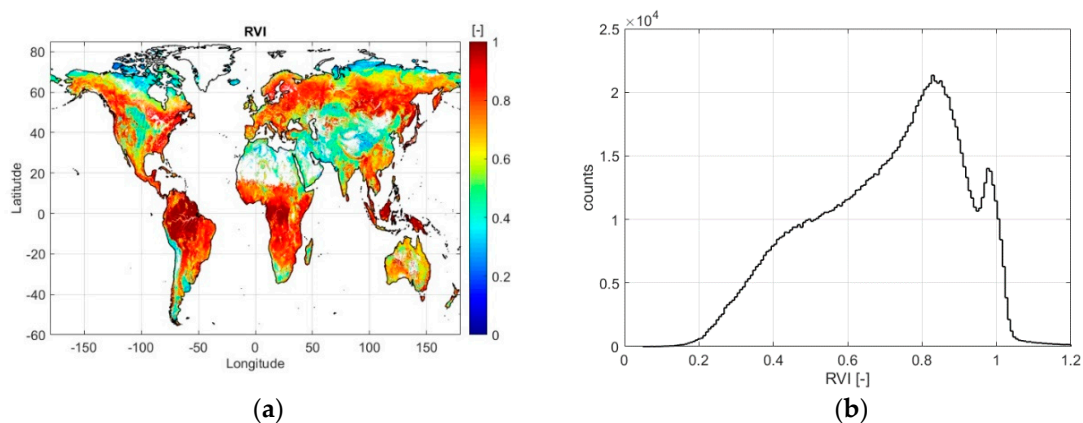


Figure 7. Result of the averaged (April–July 2015) standard RVI [-] calculated with (1): (a) global map; (b) histogram of values ranging beyond one for high amounts of biomass.

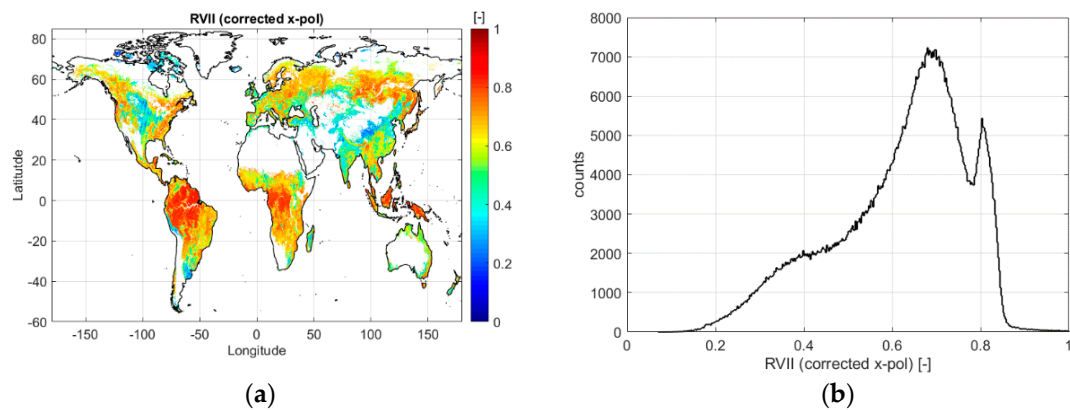


Figure 8. Result of the averaged (April–July 2015) RVII [-] calculated with (8): (a) global map; (b) histogram of values ranging only between zero and one.

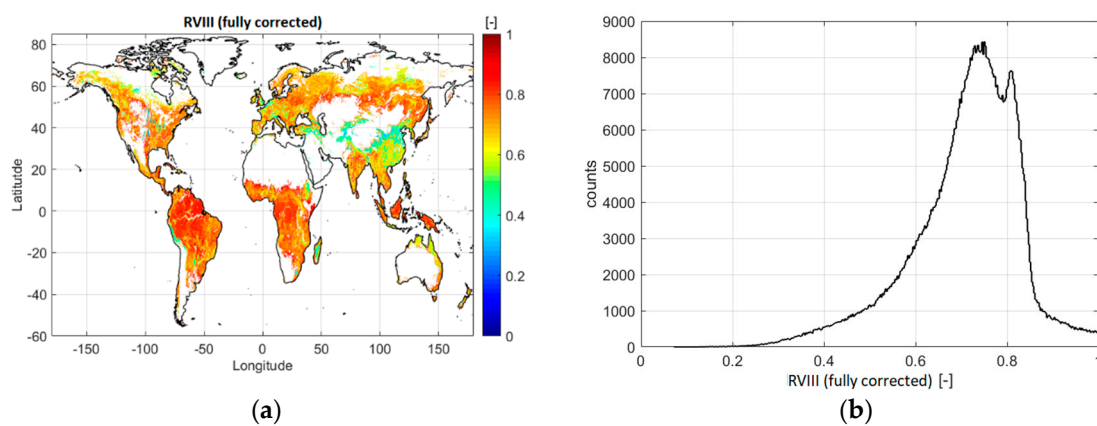


Figure 9. Result of the averaged (April–July 2015) RVIII [-] calculated with (9): (a) global map; (b) histogram of values ranging only between zero and one.

There is a general shift towards lower values of the radar vegetation index as shown in the histograms in Figures 8b and 9b. The global maximum in the histogram of the RVII is located at 0.7 and a local one can be found at 0.8. The dry and bare surfaces of Central and Western Australia show RVI-values up to 0.7 (see Figure 7a). However, these values are unlikely to be representative of the vegetation cover in the region. This is due to soil roughness-induced high values of σ_{HV}^m instead of any cross-polarization contribution from vegetation. Both RVII and RVIII remove the soil scattering contribution and, in cases where the resulting backscatter is negative, the region is considered to have a too strong surface soil contribution and is masked out. Radar-based vegetation indices at L-band are not suited (valid) for these regions.

4.2. Correlation of Radar Vegetation Indices with Soil- and Vegetation-Related Parameters

Correlations of soil related parameters are shown in Figures 10 and 11. Figure 10 demonstrates the relation between the RVI, RVII, RVIII and the volumetric soil moisture derived from SMAP radiometer measurements [18]. The data have soil moisture values that are limited to a range between 0 and 0.6 [cm³/cm³] [35]. Ideally there should be no correlation between soil moisture and the indices. The dependence on soil moisture is already small with RVI ($R^2 = 0.08$). The new indices reduce the dependence further as expected from their formulation (RVII: $R^2 = 0.06$; RVIII: $R^2 = 0.02$).

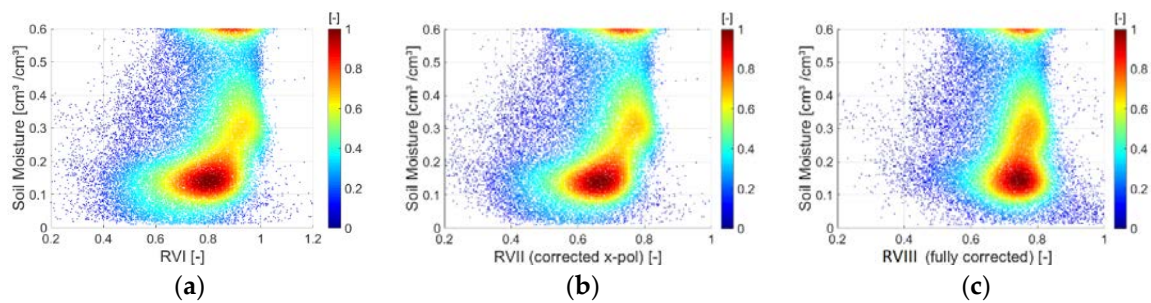


Figure 10. Correlation for the combined study areas between: (a) RVI [-]; (b) x-pol corrected RVII [-]; (c) fully corrected RVIII [-] and volumetric surface soil moisture [cm^3/cm^3] derived from SMAP [18,35].

Figure 11 shows the relation of soil roughness height standard deviation non-dimensionalized with wave-length (ks) to RVI, RVII and RVIII. The standard index (RVI) exhibits a dependency to the surface roughness parameter ($R^2 = 0.37$) as shown in Figure 11a. The relation improves (by reduction in correlation) slightly but definitely not adequately for the cross-polarization-corrected RVII ($R^2 = 0.36$) as shown in Figure 11b. The fully corrected index (RVIII) shows much reduced correlation to the soil roughness ($R^2 = 0.01$) as shown in Figure 11c. This affirms that a correction of the soil roughness contribution is necessary, as a pure vegetation-based radar vegetation index should be independent of surface roughness influences.

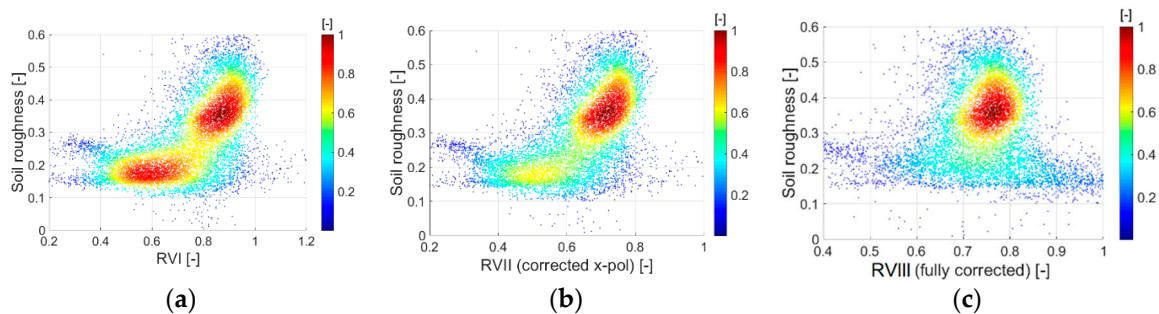


Figure 11. Correlation for the combined study areas between: (a) RVI [-]; (b) x-pol corrected RVII [-]; (c) fully corrected RVIII [-] and SMOS-based soil surface roughness (ks) [-] (derived from Parrens et al. from [19]).

The relation with vegetation-related parameters is shown in Figures 12 and 13. Figure 12 shows the correlation of the RVI, RVII and RVIII with the volumetric water content of the vegetation (VWC). Unlike the previous analyses with surface soil moisture and roughness (where the ideal was low correlation), the analysis with vegetation properties ideally show high correlation.

The scatterplots indicate a distinct link to the water content of vegetation in all three cases (RVI, RVII and RVIII). The distributions reveal a positive (linear) relationship for the standard RVI ($R^2 = 0.53$) as shown in Figure 12a. The correlation is most clearly evident for RVI between 0.5 and 1 [-]. The correlations do not improve appreciably for RVII and RVIII. All three indices are equally linked to wetness and structure of vegetation.

Results for the correlation with the plant structure and geometry-related leaf area index (LAI) are shown in Figure 13. However, the structural part of the forward modelling indicates a dependency of RVI (RVII, RVIII) to the leaf structure. The resulting scatterplots point towards a weak but positive linear relation. The statistics however show reduced correlation in the case of Figure 13c (RVI: $R^2 = 0.56$; RVII: $R^2 = 0.53$; RVIII: $R^2 = 0.35$). Hence, RVIII indicates lower sensitivity under high biomass after elimination of soil contribution than RVI and RVII. Whether LAI should be dominantly reflected in a low-frequency microwave vegetation index, from L-band waves penetrating into canopy and below the leaf layer, is open to debate. Therefore, it is likely possible that the optical LAI and the microwave

radar vegetation indices provide information about rather different volumes of the vegetation canopy. The former is more indicative of canopy leaves and their abundance [36], while the latter is also including woody elements (trunk and branch) [37].

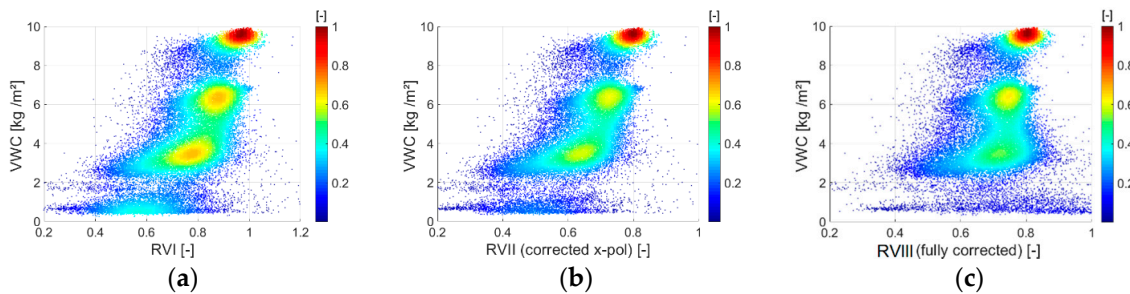


Figure 12. Correlation for the combined study areas between: (a) RVI [-]; (b) x-pol corrected RVII [-]; (c) fully corrected RVIII [-] and MODIS-based volumetric vegetation water content (VWC) [kg/m^2] [18].

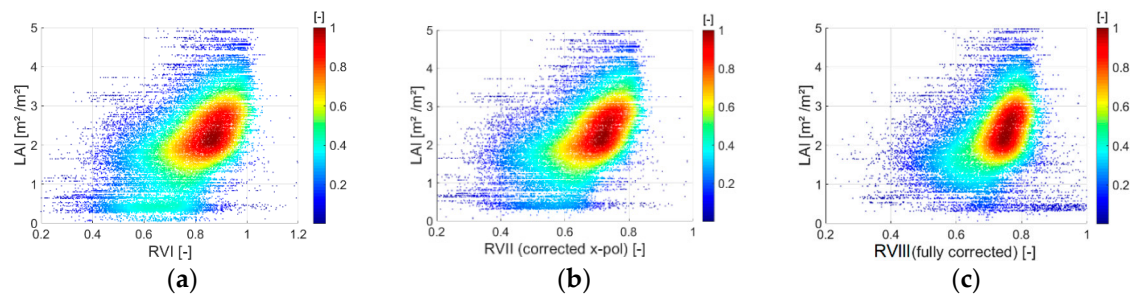


Figure 13. Correlation for the combined study areas between: (a) RVI [-]; (b) x-pol corrected RVII [-]; (c) fully corrected RVIII [-] and Leaf Area Index (LAI) [m^2/m^2] from Myneni et al. [24].

5. Summary and Conclusions

The aim of this study is to better understand the behavior of the microwave radar vegetation indices (RVI) at low microwave frequencies. We use a multi-sensor (active-passive microwave) approach to isolate vegetation and surface soil contributions to the indices. This is achieved using forward models that predict the linear backscattering intensity from the vegetation and from the soil underneath, as well as the attenuation within the vegetation. The backscatter from vegetation is calculated using a polarimetric single layer model of spheroids also known as $Ap\text{-}\psi$ model. The soil contribution originates from a polarimetric soil scattering model for longer wavelength, the extended Bragg model, which includes a passive microwave-based static map of surface roughness [19]. The vegetation attenuation estimates are also derived from passive microwaves (through the vegetation optical depth parameter) [32]. The structural and dielectric components contributing to volume scattering are estimated with a polarimetric backscattering ($Ap\text{-}\psi$) model of vegetation. Results show that the standard pre-factor in the definition of the standard RVI does not normalize the index and does not limit it to be between zero and one, which makes its interpretation difficult and applicability. A new pre-factor is found that properly normalizes RVI and it is 6.57 instead of 8 based on the forward model analyses. Two improved versions of the RVI (called RVII and RVIII) are proposed to provide a vegetation index that reduces the soil scattering contribution present in the standard index at L-band. The degree to which the radar vegetation indices isolate the volume scattering from vegetation from surface contributions is analyzed by performing correlation analyses of the indices with surface soil moisture and surface roughness estimates as well as vegetation properties.

In known sparsely or non-vegetated areas, the RVI can be as high as 0.7 [-] due to soil roughness-induced cross-polarization (σ_{HV}^m) instead of cross-polarization from vegetation. The improved indices combine active and passive microwave data to confine their dynamic range between zero and one. The new indices remove the surface contributions (scattering from rough surfaces and

surface reflectivity due to soil moisture). However, where the surface contribution is large compared to any existing vegetation, i.e., deserts, open shrublands, steppes, etc. then the residual backscatter (after removal) may become negative. This indicates a lower limit of applying microwave backscatter indices due to significant penetration of L-band waves into sparse and open canopies [38]. In this respect the microwave vegetation indices represent a different fraction of the vegetation volume than optical- and infrared-based ones. The latter indices also work in sparsely vegetated regions, but their sensitivity is significantly diminished in closed and denser canopies.

Author Contributions: C.S. carried out the data analysis and led the manuscript writing. T.J. developed the methodological framework, discussed the results with C.S. and supervised the research in all development stages. M.B. contributed to the data processing and especially on analyzing the RVI by forward modelling. C.T., J.-P.W., M.P. (Maria Piles) and D.E. supervised the research efforts. M.P. (Marie Parrens) delivered crucial soil roughness data and knowledge for the forward modelling of soil scattering. All authors compiled and approved the final manuscript.

Funding: This research received no external funding.

Acknowledgments: The authors gratefully acknowledge Stefan Kern from the Integrated Climate Data Center (ICDC) for providing the MODIS data and Kaighin McColl for discussions on RVI modeling and retrieval. The authors thank MIT for supporting this research with the MIT-Germany Seed Fund “Global Water Cycle and Environmental Monitoring using Active and Passive Satellite-based Microwave Instruments”. M.P. (Maria Piles) is supported by a Ramón y Cajal contract (MINECO). The authors want to offer here that the RVII, RVIII and the vegetation-dominance mask are available on request.

Conflicts of Interest: The authors declare no conflict of interest.

References

- Xie, Y.; Sha, Z.; Yu, M. Remote Sensing Imagery in Vegetation Mapping: A Review. *J. Plant Ecol.* **2008**, *1*, 9–23. [[CrossRef](#)]
- Xiao, X.; Zhang, Q.; Braswell, S.; Urbanski, S.; Boles, S.; Wolfsy, B.; Moore, B.; Ojima, D. Modelling gross primary production of temperate deciduous broadleaf forest using satellite and climate data. *Remote Sens. Environ.* **2004**, *91*, 256–270. [[CrossRef](#)]
- IPCC. Climate Change 2013: The Physical Science Basis. In *Contribution of Working Group I to the Fifth Assessment Report of the Intergovernmental Panel on Climate Change*; Stocker, T.F., Qin, D., Plattner, G.K., Tignor, M., Allen, S.K., Boschung, J., Nauels, A., Xia, Y., Bex, V., Midgley, P.M., Eds.; Cambridge University Press: Cambridge, MA, USA, 2013.
- Frank, D.; Reichstein, M.; Bahn, M.; Thonicke, K.; Frank, D.; Mahecha, M.D.; Smith, P.; Van der Velde, M.; Vicca, S.; Babst, F.; et al. Effects of Climate Extremes on the Terrestrial Carbon Cycle: Concepts, Processes and Potential Future Impacts. *Glob. Chang. Biol.* **2015**, *21*, 2861–2880. [[CrossRef](#)] [[PubMed](#)]
- Vereecken, H.; Weihermueller, L.; Jonard, F.; Montzka, C. Characterization of Crop Canopies and Water Stress Related Phenomena using Microwave Remote Sensing Methods: A Review. *Vadose Zone J.* **2012**, *11*. [[CrossRef](#)]
- Steele-Dunne, S.C.; McNairn, H.; Monsivais-Hubertero, A.; Judge, J.; Liu, P.-W.; Papathanassiou, K. Radar Remote Sensing of Agricultural Canopies: A Review. *Sel. Top. Appl. Earth Obs. Remote Sens.* **2017**, *10*, 2249–2273. [[CrossRef](#)]
- Entekhabi, D.; Das, N.; Yueh, S.; De Lannoy, G.; O’Neill, P.; Dunbar, R.S.; Kellogg, K.H.; Edelstein, W.N.; Allen, A.; Entin, J.K.; et al. *SMAP Handbook—Soil Moisture Active Passive—Mapping Soil Moisture and Freeze/Thaw from Space*; Jet Propulsion Laboratory: Pasadena, CA, USA, 2014.
- Ulaby, F.T.; Long, F.G.; Blackwell, W.; Elachi, C.; Fung, A.; Ruf, C.; Sarabandi, K.; Zebker, H.; Van Zyl, J. *Microwave Radar and Radiometric Remote Sensing*; Artech House: Boston, MA, USA, 2015; ISBN 9780472119356.
- Du, J.; Kimbal, J.S.; Jones, L.A.; Kim, Y.; Glassy, J.; Watts, J.D. A Global Satellite Environmental Data Record derived from AMSR-E and AMSR2 Microwave Earth Observations. *Earth Syst. Sci. Data* **2017**, *9*, 791–808. [[CrossRef](#)]
- Tao, J.; Shi, J.; Jackson, J.; Du, J.; Bindlish, R.; Zhang, L. Monitoring Vegetation Water Content using Microwave Vegetation Indices. In Proceedings of the 2008 IEEE International Symposium on Geoscience and Remote Sensing, Boston, MA, USA, 7–11 July 2008; pp. 197–200.

11. Srivastava, P.; O'Neill, P.; Cosh, M.; Lang, R.; Josph, A. Evaluation of Radar Vegetation Indices for Vegetation Water Content Estimation using Data from a Ground-Based SMAP Simulator. In Proceedings of the 2015 IEEE International Geoscience and Remote Sensing Symposium (IGARSS), Milan, Italy, 26–31 July 2015; pp. 1296–1299.
12. Motofumi, A.; van Zyl, J.; Kim, Y. A General Characterization for Polarimetric Scattering from Vegetation Canopies. *IEEE Trans. Geosci. Remote Sens.* **2010**, *48*, 3349–3357. [[CrossRef](#)]
13. McColl, K.A.; Entekhabi, D.; Piles, M. Uncertainty Analysis of Soil Moisture and Vegetation Indices using Aquarius Scatterometer Observations. *IEEE Trans. Geosci. Remote Sens.* **2013**, *52*, 4259–4272. [[CrossRef](#)]
14. Kim, Y.; Jackson, T.; Bindlish, R.; Lee, H.; Hong, S. Radar Vegetation Index for Estimating the Vegetation Water Content of Rice and Soybean. *IEEE Geosci. Remote Sens. Lett.* **2012**, *9*, 564–568. [[CrossRef](#)]
15. Kim, Y.; Jackson, T.; Bindlish, R.; Hong, S.; Jung, G.; Lee, K. Retrieval of Wheat Growth Parameters with Radar Vegetation Indices. *IEEE Geosci. Remote Sens. Lett.* **2014**, *11*, 4259–4272. [[CrossRef](#)]
16. Huang, Y.; Walker, J.P.; Gao, Y.; Wu, X.; Moneris, A. Estimation of Vegetation Water Content from the Radar Vegetation Index at L-band. *IEEE Trans. Geosci. Remote Sens.* **2015**, *54*, 981–989. [[CrossRef](#)]
17. Belward, E.A. The IGBP-DIS global 1 km Land Cover Dataset “DISCover”: Proposal and Implementation Plans. In *Report of the Land Cover Working Group of the IGBP-DIS. IGBP-DIS Working Paper*; IGBP-DIS Office: Stockholm, Sweden, 1996.
18. Entekhabi, D.; Das, N.; Njoku, E.G.; Johnson, J.T.; Shi, J. *SMAP L3 Radar/Radiometer Global Daily 9 km EASE-Grid Soil Moisture*; Version 3; NASA National Snow and ICE Data Center Distribution Active Archive Center: Boulder, CO, USA, 2016. [[CrossRef](#)]
19. Parrens, M.; Wigneron, J.-P.; Richaume, P.; Mialon, A.; Al Bitar, A.; Fernandez-Moran, R.; Al-Yaari, A.; Kerr, Y.H. Global-Scale Surface Roughness Effects at L-band as Estimated from SMOS observations. *Remote Sens. Environ.* **2016**, *181*, 122–136. [[CrossRef](#)]
20. Kerr, Y.H.; Waldteufel, P.; Wigneron, J.-P.; Martinuzzi, J.-M.; Font, J.; Berger, M. Soil Moisture Retrieval from Space: The Soil Moisture and Ocean Salinity (SMOS) Mission. *IEEE Trans. Geosci. Remote Sens.* **2001**, *39*, 727–744. [[CrossRef](#)]
21. Kerr, Y.H.; Al-Yaari, A.; Rodriguez-Fernandez, N.; Parrens, M.; Molero, B.; Leroux, D.; Bircher, S.; Mahmoodi, A.; Mialon, A.; Richaume, P.; et al. Overview of SMOS Performance in Terms of Global Soil Moisture Monitoring after Six Years in Operation. *Remote Sens. Environ.* **2016**, *180*, 40–63. [[CrossRef](#)]
22. Wigneron, J.-P.; Jackson, T.J.; O'Neill, P.; De Lannoy, G.; De Rosnay, P.; Walker, J.P.; Ferrazzoli, P.; Mironov, V.; Bircher, S.; Grant, J.P.; et al. Modelling the Passive Microwave Signature from Land Surfaces: A Review of Recent Results and Application to the L-band SMOS & SMAP Soil Moisture Retrieval Algorithms. *Remote Sens. Environ.* **2017**, *192*, 238–262. [[CrossRef](#)]
23. Chan, S.; Bindlish, R.; Hunt, R.; Jackson, T.; Kimball, J.S. *SMAP Ancillary Data Report Vegetation Water Content*; Version 1; Jet Propulsion Laboratory: Pasadena, CA, USA, 2013.
24. Myneni, R.; Knyazikhin, Y.; Park, T. *MOD15A2H MODIS/Terra Leaf Area Index/FPAR 8-Day L4 Global 500 m SIN Grid V006*; Version 6; NASA EOSDIS Land Processes DAAC: Boulder, CO, USA, 2015.
25. Myneni, R.; Knyazikhin, Y.; Glassy, J.; Votova, P.; Shabanov, N. *FPAR, LAI (ESDT:MOD15A2) 8-Day Composite NASA MODIS Land Algorithm*; Terra MODIS Land Team: Greenbelt, MD, USA, 2003.
26. Kim, Y.; van Zyl, J. On the Relationship between Polarimetric Parameters. In Proceedings of the 2000 IEEE International Symposium on Geoscience and Remote Sensing, Honolulu, HI, USA, 24–28 July 2000; pp. 1298–1300.
27. Jagdhuber, T. *Soil Parameter Retrieval under Vegetation Cover Using SAR Polarimetry*; University of Potsdam: Potsdam, Germany, 2012.
28. Cloude, S.R. *Polarisation: Applications in Remote Sensing*; Oxford University Press: Oxford, UK, 2010; ISBN 9780199569731.
29. Ulaby, F.T.; El-Rayes, M.A. Microwave dielectric spectrum of vegetation-Part II: Dual-dispersion model. *IEEE Trans. Geosci. Remote Sens.* **1987**, *GE-25*, 550–557. [[CrossRef](#)]
30. Van de Hulst, H.C. *Light Scattering by Small Particles*; Dover Publications: Dover, UK, 1981; ISBN 9780486642284.
31. Bohren, C.F.; Huffman, D.R. *Absorption and Scattering of Light by Small Particles*; Wiley: Weinheim, Germany, 2004; ISBN 9780471293408.

32. Konings, A.G.; Piles, M.; Rötzer, K.; McColl, K.; Chan, S.K.; Entekhabi, D. Vegetation Optical Depth and Scattering Albedo Retrieval using Time Series of Dual-Polarized L-band Radiometer Observations. *Remote Sens. Environ.* **2016**, *172*, 178–189. [[CrossRef](#)]
33. Hajnsek, I.; Pottier, E.; Cloude, S.R. Inversion of Surface Parameters from Polarimetric SAR. *IEEE Trans. Geosci. Remote Sens.* **2003**, *41*, 727–744. [[CrossRef](#)]
34. Mironov, V.L.; Fomin, S.V. Temperature and Mineralogy Dependable Model for Microwave Dielectric Spectra of Moist Soils. *PIERS Online* **2009**, *5*, 411–415. [[CrossRef](#)]
35. Das, N.N.; Scott Dunbar, R. *SMAP Level 3 Active/Passive Soil Moisture Product Specification Document*; Jet Propulsion Laboratory: Pasadena, CA, USA, 2015.
36. Zheng, G.; Moskal, L.M. Retrieving Leaf Area Index (LAI) using Remote Sensing: Theories, Methods and Sensors. *Sensors* **2009**, *9*, 2719–2745. [[CrossRef](#)] [[PubMed](#)]
37. Le Toan, T.; Beaudoin, A.; Riom, J.; Guyon, D. Relating Forest Biomass to SAR Data. *IEEE Trans. Geosci. Remote Sens.* **1992**, *30*, 403–411. [[CrossRef](#)]
38. Baur, M.; Jagdhuber, T.; Link, M.; Piles, M. Multi-Frequency Estimation of Canopy Penetration Depths from SMAP/AMSR2 Radiometer and IceSAT Lidar Data. In Proceedings of the IEEE International Symposium Geoscience and Remote Sensing, Valencia, Spain, 23–27 July 2018.



© 2018 by the authors. Licensee MDPI, Basel, Switzerland. This article is an open access article distributed under the terms and conditions of the Creative Commons Attribution (CC BY) license (<http://creativecommons.org/licenses/by/4.0/>).